Design and simulation of the snowflake divertor control for NSTX–U

P. J. Vail[a,*], M. D. Boyer[b], A. S. Welander[c], E. Kolemen[a,**]

[a] *Department of Mechanical and Aerospace Engineering, Princeton University, Princeton, New Jersey, USA*
[b] *Princeton Plasma Physics Laboratory, Princeton, New Jersey, USA*
[c] *General Atomics, San Diego, California, USA*

Abstract

This paper presents the development of a physics-based multiple-input-multiple-output algorithm for real-time feedback control of snowflake divertor (SFD) configurations on the National Spherical Torus eXperiment Upgrade (NSTX–U). A model of the SFD configuration response to applied voltages on the divertor control coils is first derived and then used, in conjunction with multivariable control synthesis techniques, to design an optimal state feedback controller for the configuration. To demonstrate the capabilities of the controller, a nonlinear simulator for axisymmetric shape control was developed for NSTX–U which simultaneously evolves the currents in poloidal field coils based upon a set of feedback-computed voltage commands, calculates the induced currents in passive conducting structures, and updates the plasma equilibrium by solving the free-boundary Grad-Shafranov problem. Closed-loop simulations demonstrate that the algorithm enables controlled operations in a variety of SFD configurations and provides capabilities for accurate tracking of time-dependent target trajectories for the divertor geometry. In particular, simulation results suggest that a time-varying controller which can properly account for the evolving SFD dynamical response is not only desirable but necessary for achieving acceptable control performance. The algorithm presented in this paper has been implemented in the NSTX–U Plasma Control System in preparation for future control and divertor physics experiments.

1. Introduction

The National Spherical Torus eXperiment Upgrade (NSTX–U) [1], which conducted its initial campaign of plasma operations in 2016 [2, 3], is a mega-ampere grade spherical tokamak (ST) at the Princeton Plasma Physics Laboratory (PPPL) that has been commissioned to enhance the physics and engineering understanding required for building future ST-based fusion devices, such as those intended for studying plasma-material interactions [4], testing nuclear reactor components [5], and demonstrating fusion power generation [6]. NSTX–U is designed to improve upon the performance of prior STs such as NSTX [7] and the Mega-Ampere Spherical Tokamak (MAST) [8] and will enable access to new plasma regimes for the study of critical issues such as the scaling of energy confinement with electron collisionality [9], the physics of fast particles [10], and the efficiency of methods for non-inductive current drive in high-β scenarios [11]. NSTX–U received significant hardware upgrades prior to its commissioning, including the installation of a larger-diameter centerstack and a second neutral beam injection (NBI) system. The new centerstack, which contains the inner legs of the toroidal field (TF) coils, the Ohmic heating (OH) solenoid, and several plasma shaping coils, provides higher fluxes and fields for increasing plasma confinement and extending the duration of plasma discharges. The second NBI system increases the auxiliary heating power (from 5 to 10 MW) and current drive and is aimed more tangentially, thereby enabling greater control of the spatial distribution of heating and current. The upgrades will increase the nominal TF from 0.5 to 1T, the maximum plasma current from 1 to 2 MA, and will enable plasma discharge durations of up to 5s.

1.1. Motivation for advanced divertors on NSTX–U

Routine plasma operations in high-performance scenarios (2 MA, 1T, 10 MW) is a crucial prerequisite for achieving many of the goals of the NSTX–U research program. As a primary example, higher plasma current and toroidal field are required on NSTX–U to distinguish between conventional aspect ratio and ST confinement time scaling, and a corresponding increase in input heating power is required for achieving sufficient plasma-β at these higher currents and fields. Furthermore, a target discharge duration of 5s is motivated by a need to ensure sufficient current profile equilibration in high confinement, low density plasma regimes [12]. A consequence of these device requirements is that a variety of novel technologies and operational strategies will be needed in the coming years for achieving safe and reliable high-performance discharges on NSTX–U. Since the early stages of the upgrade, it has been recognized that one of the most critical issues for

*Corresponding author 1
**Corresponding author 2
Email addresses: pjv@princeton.edu (P. J. Vail), ekolemen@princeton.edu (E. Kolemen)

NSTX–U will be the power loading of plasma-facing components (PFCs) in the divertor region. While heat flux management is a concern for many current and future devices, it is of particular importance for STs due to their compact size. In [1], it was shown that in the NSTX–U high-performance scenario with 2 MA, 10 MW, and 5s pulse length, the peak heat flux on divertor surfaces cannot exceed 10 MW/m^2 without compromising the structural integrity of the radiatively-cooled PFCs. Since the start of NSTX–U plasma operations, the requirements for heat flux mitigation have grown more stringent as the design of the divertor PFCs is re-evaluated during the NSTX–U recovery project. This analysis incorporates more recent developments in the fusion community, including the identification of significant uncertainty in the scaling of the heat flux width λ_q for STs. Indeed, the projected values of λ_q for NSTX–U as computed by several recently-proposed empirical and semi-empirical models vary by up to a factor of two [13–16], thereby leading to a corresponding uncertainty in the peak heat flux deposited on the divertor.

A combination of heat flux mitigation strategies is currently planned for use on NSTX–U, including controlled sweeping of the divertor strike points to vary the location of peak power loading, operating in a double-null configuration to enable sharing of the power exhaust between the up-down symmetric divertor PFCs, and adding divertor fueling capabilities to increase the radiated power fraction. Another promising means of reducing the peak heat flux on divertor PFCs is the use of so-called advanced divertor configurations, such as the snowflake divertor [17], X-divertor [18], super-X divertor [19], and X-point target divertor [20], all of which are magnetic topologies that differ in some way from that of the conventional single-null (SN) divertor. In particular, the snowflake divertor (SFD) is being considered as one component of an integrated power exhaust solution on NSTX–U. The exact SFD configuration has a second-order null on the primary separatrix and is characterized by a magnetic topology with a hexagonal structure resembling a snowflake. Due to the extreme sensitivity of the exact SFD to small deviations from the magnetic field distribution that defines this equilibrium, one of two alternative configurations is generally observed: (1) the SFD-plus with a secondary X-point in the private flux region, and (2) the SFD-minus in which the secondary X-point lies in the scrape-off layer (SOL). Figure 1 depicts three simulated snowflake equilibria on NSTX–U, including the required coil currents for each configuration, as well as a conventional SN equilibrium for comparison.

As summarized in [21], the SFD has several properties that are advantageous for reducing divertor PFC heat fluxes: Due to the reduced poloidal field (PF) magnitude in the null region, the SFD exhibits stronger flaring of magnetic fieldlines and increased poloidal flux expansion relative to the standard divertor. The result is a greatly increased plasma wetted-area and a corresponding decrease in the peak heat flux. The need for high flux expansion divertors to mitigate power exhaust is the primary motivation for the development of SFD scenarios on NSTX–U. Additional properties of the configuration include a significantly longer X-point connection length, leading to an increase in the temperature drop and radiative losses in the SOL, and the presence of additional strike points across which the power exhaust can be partitioned. In recent years, the SFD has been the subject of investigations on several devices [22–29], all of which have provided experimental confirmation of many favorable properties of the configuration. In particular, the SFD was integrated into H-mode scenarios on NSTX (prior to the upgrade). Equilibrium reconstructions of 1 MA, 0.5T, 5 MW NBI-heated discharges revealed that the flux expansion in the SFD was nearly four times higher than in the conventional SN divertor, while the X-point connection length was double that of the SN configuration [27]. The existence of these favorable magnetic properties was accompanied by a significant reduction in the peak heat flux on the divertor (from roughly 5 to 1 MW/m^2) as measured by infrared diagnostics for the discharges investigated in [27]. Furthermore, no degradation of core and pedestal performance, as quantified by metrics such as confinement time, β_N, and stored energy, was exhibited during plasma operations in the SFD configuration. Recent research efforts have focused on generating SFD scenarios for NSTX–U with free-boundary equilibria design codes and developing edge plasma simulations to study advanced divertor

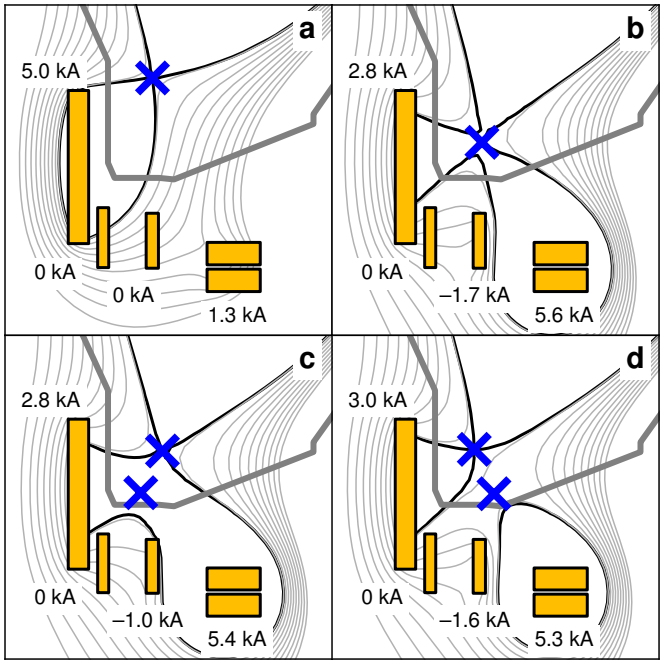

Figure 1: Several divertor configurations on NSTX–U as computed by a free-boundary equilibrium solver with $I_p = 1$ MA, $\beta_p = 1.0$, and $l_i = 0.6$. Shown are (a) the standard single-null divertor, (b) the exact snowflake configuration with a second-order null, (c) the snowflake-plus configuration with a secondary null in the private flux region, and (d) the snowflake-minus configuration with a secondary null in the scrape-off layer. Also shown are the divertor coils (yellow) and coil currents for each configuration.

physics relevant for future NSTX–U plasma operations. Using the free-boundary equilibrium code ISOLVER [30], it was demonstrated that a large range of snowflake configurations can be created with the NSTX–U divertor coils for a variety of plasma currents and Ohmic flux states and without exceeding the divertor coil current limits [31]. Furthermore, numerical simulations with the multi-fluid edge transport code UEDGE [32] have suggested, for instance, that conventional single-null divertors with large flux expansions similar to the SFD may enable a more gradual transition to detachment than divertors with standard flux expansions [33]. Future experiments will seek to assess the performance of the SFD at the higher currents, fields, and input heating powers that are projected for NSTX–U.

1.2. Overview of magnetic control for the SFD

While the SFD may prove to be an enabling technology for NSTX–U (as well as for future devices such as ITER [34] and DEMO [35]) due to its favorable magnetic properties, the snowflake configuration presents new challenges for real-time plasma operations: Due to the sensitivity of the second-order field null in the exact SFD, one must normally account for the locations of two proximate X-points, both of which are candidates for the null which defines the magnetic flux on the plasma boundary, in either the SFD-plus or SFD-minus. While of little consequence for the global shape and positioning of the plasma due to the shallow field gradients in the vicinity of the X-points, the identity of the boundary-defining point in the SFD has a significant impact on divertor performance as a modification of the boundary flux can cause a large shift in the locations of active strike points. Furthermore, the relative positioning of the two X-points determines critical SFD properties such as flux expansion, connection length, and power exhaust partitioning across multiple divertor legs. In addition to the geometric complexities of the configuration, the SFD is a particularly challenging dynamical system to control as the response of the configuration to changes in the divertor coil currents is a strongly nonlinear function of the relative positioning of the two X-points. Furthermore, it is often the case that fewer shape control coils are available on a particular device than are required for simultaneous control of all parameters that define the divertor configuration. On many devices such as NSTX–U, there is also significant cross-coupling between divertor control coils. The unique challenges presented by the SFD motivate the development of a sophisticated multiple-input-multiple-output (MIMO) feedback control algorithm which is capable of accurately tracking the positions of the two X-points and properly accounting for the time-evolving dynamical response of the configuration.

Over the last several years, various solutions to the SFD control problem have been tested experimentally. TCV has used extensive offline modeling to determine coil currents that are consistent with desired snowflake equilibria [22]. The coil currents are then pre-programmed as targets for the control system to track during real-time operations. On NSTX, the first experiments in which the SFD configuration was achieved employed a combined feedforward-feedback hybrid approach in which the primary divertor coils were used to control the locations of the inner and outer strike points, while the currents in secondary coils were modified in a gradient-search fashion to determine values of the plasma squareness ζ and $\delta R_{\rm sep}$ that were consistent with a SFD equilibrium [26, 36]. Based upon modeling of SFD configurations on NSTX using ISOLVER, it was determined that the use of three divertor coils would enable refined control. In further experiments on NSTX, therefore, a primary coil was used in a feedback loop to control the location of the primary X-point, while two secondary coils executed pre-programmed current ramps to push the secondary X-point into the vacuum vessel [27]. These combined feedforward-feedback approaches on NSTX were sufficient for achieving transient snowflakes but were unable to mitigate the effects of disturbances such as variations in the plasma inductance, edge current, and eddy currents in divertor structures. The first entirely closed-loop feedback algorithm was developed and deployed on DIII–D [37]. The control scheme was capable of locating the SFD in real-time using a non-iterative X-point finder based upon series expansions of the magnetic field structure in the divertor region. A linearized model relating changes in the divertor coil currents to changes in the snowflake geometry was used in-the-loop to compute the coil currents required for achieving a desired equilibrium. The algorithm enabled reliable control of the inter-null distance in both the SFD-plus and SFD-minus configurations and provided some functionality for simultaneous control of the X-point separation distance and angular orientation.

While much progress has been made toward the development of an advanced feedback control system for the SFD, the performance of prior control schemes has been limited due to several factors: Previous controllers have all employed some form of proportional-integral-derivative (PID) [38] control law with static gains that were empirically-tuned to yield acceptable controller performance on the target equilibrium. This approach, while having enabled sufficient control of the SFD for initial experiments, is unlikely to yield further improvements in performance due to the inability of traditional PID-based control schemes to compensate for nonlinearities in the SFD configuration response. While design techniques such as gain-scheduling [39] exist to enable PID control of nonlinear systems, such approaches use algorithms for gain calculation which are not readily applicable to MIMO controllers. The efficacy of prior SFD control schemes has also been limited by their inability to distinguish between, and control independently, the positions of the primary and secondary nulls. As described in [37], this deficiency has been the source of significant ambiguity in recent work on DIII–D. In particular, there exist two distinct magnetic configurations that are classified as SFD-minus, one in which the secondary X-point lies in the low-field-side

(LFS) SOL and another in which the secondary X-point lies in the high-field-side (HFS) SOL. It was observed on DIII–D that the SFD-minus may transition unpredictably between these two configurations if the control system is not specifically configured to prevent this behavior.

1.3. Paper outline

In this paper, we present a physics-based, multiple-input-multiple-output algorithm that has been developed for real-time feedback control of SFD configurations on NSTX–U. In Section 2, we derive a linear time-varying (LTV) model that describes the response of the SFD geometric configuration to applied voltages on the divertor control coils. The primary components of the model are a set of coupled circuit equations describing the time-dynamics of the coil currents, a series approximation that models the response of an X-point position to changes in PF structure, and a linearized model of the plasma response to changes in the PF coil currents. In Section 3, we use the LTV model along with standard multivariable control synthesis techniques to design an optimal state feedback controller for the configuration. In Section 4, we describe a nonlinear axisymmetric shape control simulator that was developed for NSTX–U which simultaneously evolves the currents in PF coils based upon a set of feedback-computed voltage commands, calculates the induced currents in passive conducting structures, and updates the plasma equilibrium by solving the free-boundary Grad-Shafranov problem. We then present the results of time-dependent, closed-loop simulations in which the controller was used to achieve and transition between a variety of SFD equilibria of interest for future NSTX–U operations. Finally, in Section 5, we summarize our work and discuss plans for future control development.

2. System modeling for the SFD

The typical starting point for any control system design is the generation and validation of a model that describes the system dynamics of interest with sufficient accuracy. For this work, we seek a model that accurately describes the time-response of a set of geometric parameters that defines the snowflake configuration to applied voltages on the divertor control coils. In particular, our goal is to derive an LTV model in so-called state-space form,

$$\delta\dot{\mathbf{x}} = \mathbf{A}(t)\,\delta\mathbf{x} + \mathbf{B}(t)\,\delta\mathbf{v}, \tag{1a}$$

$$\delta\mathbf{y} = \mathbf{C}(t)\,\delta\mathbf{x}, \tag{1b}$$

where $\mathbf{v}$ is a vector that contains the values of the system inputs, $\mathbf{y}$ is a vector that contains measurements of the system outputs, and $\mathbf{x}$ is a vector that contains a set of parameters that uniquely defines the dynamical state of the system. We note that the elements of $\mathbf{x}$ are, in general, not directly measureable. The state-space modeling formalism is particularly well-suited to the SFD due to the compatibility of state-space models with systematic control design methods for MIMO systems which have multiple actuators and controlled variables. For the SFD, it will be shown in Section 2.1 that the inputs $\mathbf{v}$ are the coil voltages, the states $\mathbf{x}$ are the coil currents, and the outputs $\mathbf{y}$ are the parameters defining the SFD geometry. In (1a) and (1b), the symbol δ indicates that the aforementioned vectors are measured relative to their values at some initial condition. For the LTV model of the SFD configuration, the initial condition will always be a set of PF coil currents and steady-state voltages that defines a plasma equilibrium. Our primary task for the duration of this section is to identify the components of the time-dependent matrices $\mathbf{A}(t)$, $\mathbf{B}(t)$, and $\mathbf{C}(t)$ for the SFD system.

Two common approaches to model identification are the data-based method [40, 41] and the method which employs simplified physical arguments [42, 43]. In this paper, we choose to develop a model for the SFD based upon simplified physics as the resulting state-space model can be adapted for use in a variety of plasma scenarios and machine configurations with only minimal modifications. In particular, if the resulting model can be made sufficiently tractable, it is feasible that the model parameters and controller gains may be updated in real-time within the control system to account for the evolving plasma equilibrium. As discussed in Section 1, the absence of this capability was a significant limitation of prior PID-based control algorithms for the SFD. Indeed, it will be shown in Section 4 that control system performance deteriorates significantly in certain SFD equilibria if the LTV model and corresponding controller gains are not updated with sufficient frequency.

The control algorithm described in this paper uses three divertor PF coils as actuators for the SFD configuration. One of the notable aspects of the upgrade to NSTX was the installation of a new set of PF coils in both the upper and lower divertor regions of the device, as depicted in Figure 2 for the lower divertor. The upgraded coil sets include an additional coil in each divertor region, relative to the coil configuration on NSTX prior to the upgrade, that were specifically designed for control of advanced divertor configurations such as the SFD. The additional coils provide improved shaping capabilities and are particularly important for maintaining the SFD configuration at the coil current limits of the Ohmic solenoid (± 24 kA) during long-pulse inductive scenarios. As the PF1b coils will likely be unavailable during the next several years of NSTX–U plasma operations, we have chosen to use the PF1a, PF1c, and PF2 coils as actuators for SFD control. In this paper, we develop an algorithm for control of equilibria in the lower divertor of NSTX–U and therefore will use the PF1aL, PF1cL, and PF2L coils. However, the algorithm is directly applicable to control of upper divertor snowflakes as NSTX–U is up-down symmetric.

The duration of this section is organized as follows: In Section 2.1, we present the derivation of an equation of the form (1a) that describes the dynamics of the PF coils

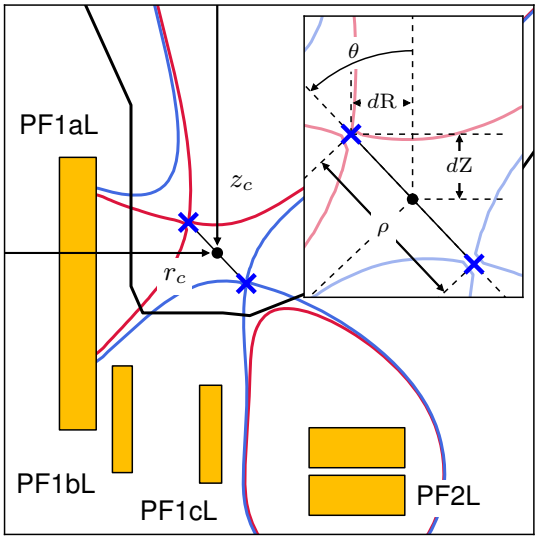

Figure 2: Illustration of the lower divertor on NSTX–U depicting the primary (red) and secondary (blue) separatrices of a snowflake divertor (SFD) and their corresponding X-points. Shown also are the limiter surface (black contour) and the poloidal field coils (yellow) available for control, namely, PF1aL, PF1bL, PF1cL, and PF2L. Labeled are the major radius r_c and vertical position z_c of the SFD centroid and the radial dR and vertical dZ displacements of the primary X-point from the centroid. The set of parameters $\{r_c, z_c, d\mathrm{R}, d\mathrm{Z}\}$ is used to specify the geometry of the SFD in the control system. Labeled also are the X-point separation distance ρ and angular orientation θ, both are which are referenced in Section 4.

used to control the SFD on NSTX–U. The modeling framework presented in this section is widely used for tokamak magnetic control design and is discussed extensively elsewhere [44, 45]. We provide an outline of the modeling approach as the results will be needed for design of the controller in Section 3. In Sections 2.2 and 2.3, we continue the development by deriving (1b) for the SFD system.

2.1. Linear MIMO model for SFD control

Our goal is to derive a model that accurately describes the dynamics which are relevant for control of the magnetic geometry in the divertor. As the axisymmetric plasma shape and divertor configuration are determined, in general, by the instantaneous values of all toroidal electric currents in the system, the primary dynamics of interest are the time responses of the currents in all toroidally-axisymmetric conductors to applied voltages on the PF coils. To simplify the model used for control design, we include only the equations for currents in divertor control coils and neglect the non-divertor coil currents as well as currents induced in any nearby conducting structures such as the vacuum vessel. We will, however, include the non-divertor coil currents and induced currents in a higher fidelity model used in Section 4 for system simulation and controller validation.

To derive the equations which govern the divertor coil dynamics, we employ a standard formalism in the field of tokamak magnetic control in which the coils are modeled as inductively-coupled, lumped parameter circuits,

$$\mathbf{M_{cc}}\dot{\mathbf{I}}_\mathbf{c} + \dot{\mathbf{\Psi}}_\mathbf{cp} + \mathbf{R_c}\mathbf{I_c} = \mathbf{V_c}, \tag{2}$$

where $\mathbf{M_{cc}}$ is the coil-to-coil mutual inductance matrix, $\mathbf{R_c}$ is a diagonal matrix containing the resistances of the coil circuits, $\mathbf{I_c}$ and $\mathbf{V_c}$ are vectors containing the currents within and voltages applied to the divertor coils, respectively, and $\dot{\mathbf{\Psi}}_\mathbf{cp}$ represents the change in magnetic flux at the coils due to spatial redistribution of the plasma current. In general, the term $\dot{\mathbf{\Psi}}_\mathbf{cp}$ is a nonlinear function of the coil and plasma currents and must be determined by solving the free-boundary Grad-Shafranov problem. To obtain an LTV model of the form (1a) and (1b), we linearize $\dot{\mathbf{\Psi}}_\mathbf{cp}$ around a reference plasma equilibrium as follows,

$$\mathbf{M_{cc}}\delta\dot{\mathbf{I}}_\mathbf{c} + \left(\left.\frac{\partial \mathbf{\Psi_{cp}}}{\partial \mathbf{I_c}}\right|_{\mathrm{eq}(t)}\right)\delta\dot{\mathbf{I}}_\mathbf{c} + \mathbf{R_c}\delta\mathbf{I_c} = \delta\mathbf{V_c}, \tag{3}$$

where we have shifted the coordinate system origin such that the coil currents $\mathbf{I_c}$ and voltages $\mathbf{V_c}$ are measured relative to their equilibrium values. The quantities $\delta\mathbf{I_c}$ and $\delta\mathbf{V_c}$ must remain small to ensure the validity of the linearization. By re-arranging the expression in (3), we find that,

$$\widehat{\mathbf{M}}(t)\delta\dot{\mathbf{I}}_\mathbf{c} + \mathbf{R_c}\delta\mathbf{I_c} = \delta\mathbf{V_c}, \tag{4}$$

where we have defined,

$$\widehat{\mathbf{M}}(t) = \mathbf{M_{cc}} + \left.\frac{\partial \mathbf{\Psi_{cp}}}{\partial \mathbf{I_c}}\right|_{\mathrm{eq}(t)}, \tag{5}$$

which is a combination of a time-independent matrix $\mathbf{M_{cc}}$, which contains the vacuum mutual inductances between the divertor coils, and a matrix $\partial_{\mathbf{I_c}}\mathbf{\Psi_{cp}}$, which represents an effective mutual inductance due to magnetic flux changes that result from a redistribution of the plasma current. The matrix $\partial_{\mathbf{I_c}}\mathbf{\Psi_{cp}}$ is, in general, time-dependent as the response of the plasma may change as the discharge evolves. We discuss several approaches to computing this response matrix in Section 2.3. The expression (4) is simple to convert into the state-space form (1a),

$$\delta\dot{\mathbf{I}}_\mathbf{c} = \mathbf{A}(t)\delta\mathbf{I_c} + \mathbf{B}(t)\delta\mathbf{V_c}, \tag{6}$$

where the matrices $\mathbf{A}(t)$ and $\mathbf{B}(t)$ are defined as follows,

$$\mathbf{A}(t) = -\left[\widehat{\mathbf{M}}(t)\right]^{-1}\mathbf{R_c}, \tag{7a}$$

$$\mathbf{B}(t) = \left[\widehat{\mathbf{M}}(t)\right]^{-1}, \tag{7b}$$

and the coil currents and voltages in vectors $\delta\mathbf{I_c}$ and $\delta\mathbf{V_c}$ are measured relative to their values in the equilibrium that was used to compute the response $\partial_{\mathbf{I_c}}\mathbf{\Psi_{cp}}$.

To derive equation (1b), we must first define the vector $\mathbf{y}$ by identifying a suitable set of model outputs that we wish to control directly. For the SFD, we choose to control the Cartesian coordinates of the snowflake centroid,

denoted as (r_c, z_c), as well as the parameters $(d\mathrm{R}, d\mathrm{Z})$, which are the radial and vertical displacements of the primary X-point from the centroid. By explicitly controlling the location of the primary X-point, we aim to eliminate many of the undesirable behaviors that were observed on DIII–D due to the lack of independent X-point control. It will be shown in Section 4 that direct control of the primary X-point location enables operations in and controlled transitioning between the LFS SFD-minus and HFS SFD-minus on NSTX–U. We note that the set $\{r_c, z_c, d\mathrm{R}, d\mathrm{Z}\}$ does not provide a unique parameterization of the SFD magnetic geometry. Two other shape parameters which will be referenced in this work are the X-point separation distance ρ and angular orientation θ. An illustration of all snowflake shape descriptors used in this paper is provided in Figure 2.

After selecting the set of snowflake shape descriptors, we can define the output matrix $\mathbf{C}(t)$ in (1b) as follows,

$$\mathbf{C}(t) = \begin{bmatrix} \partial_{\mathbf{I_c}} r_c \\ \partial_{\mathbf{I_c}} z_c \\ \partial_{\mathbf{I_c}} d\mathrm{R} \\ \partial_{\mathbf{I_c}} d\mathrm{Z} \end{bmatrix}, \tag{8}$$

where the operator $\partial_{\mathbf{I_c}}$ denotes partial differentiation with respect to each of the control coil currents. Each row of $\mathbf{C}(t)$ can be computed separately as follows,

$$\partial_{\mathbf{I_c}} r_c = \partial_{\mathbf{B}} r_c \ \left(\partial_{\mathbf{I_c}}\mathbf{B} + \partial_{\mathbf{J}}\mathbf{B} \cdot \partial_{\mathbf{I_c}}\mathbf{J}\right), \tag{9a}$$
$$\partial_{\mathbf{I_c}} z_c = \partial_{\mathbf{B}} z_c \ \left(\partial_{\mathbf{I_c}}\mathbf{B} + \partial_{\mathbf{J}}\mathbf{B} \cdot \partial_{\mathbf{I_c}}\mathbf{J}\right), \tag{9b}$$
$$\partial_{\mathbf{I_c}} d\mathrm{R} = \partial_{\mathbf{B}} d\mathrm{R} \left(\partial_{\mathbf{I_c}}\mathbf{B} + \partial_{\mathbf{J}}\mathbf{B} \cdot \partial_{\mathbf{I_c}}\mathbf{J}\right), \tag{9c}$$
$$\partial_{\mathbf{I_c}} d\mathrm{Z} = \partial_{\mathbf{B}} d\mathrm{Z} \left(\partial_{\mathbf{I_c}}\mathbf{B} + \partial_{\mathbf{J}}\mathbf{B} \cdot \partial_{\mathbf{I_c}}\mathbf{J}\right). \tag{9d}$$

In (9a) through (9d), the first terms that contain partial derivatives $\partial_{\mathbf{B}}$ represent the linearized responses of the snowflake shape descriptors to changes in the poloidal magnetic field. The terms in parentheses that contain partial derivatives $\partial_{\mathbf{I_c}}$ represent the linearized response of the poloidal magnetic field to changes in the control coil currents. This response consists of two distinct components: The term $\partial_{\mathbf{I_c}}\mathbf{B}$ represents the direct response of the field to coil current changes and is independent of the plasma configuration. The elements of $\partial_{\mathbf{I_c}}\mathbf{B}$ can be computed from the mutual inductances between the coils and a spatial grid of points at which the field is evaluated. In (9a) through (9d), the term $\partial_{\mathbf{J}}\mathbf{B}$ represents the linear change in poloidal field that results from a redistribution of the plasma current (which is caused by changing the coil currents), while $\partial_{\mathbf{I_c}}\mathbf{J}$ quantifies the change in plasma current distribution due to the coils. These values must be computed from an assumed model of the plasma response. We discuss several methods for performing this calculation in Section 2.3.

2.2. Modeling of the X-point position response

In order to determine analytical formulas for the linearized responses of the snowflake shape descriptors to changes in the poloidal field, we compute the response of a standard first-order null and then use this expression to determine the responses of the two nulls of the SFD configuration. One method for obtaining an analytical formula for the X-point response is to first approximate the field structure in the vicinity of the null by solving the toroidal component of Ampère's law,

$$(r_0 + x)\frac{\partial}{\partial x}\left(\frac{1}{r_0 + x}\frac{\partial \psi}{\partial x}\right) + \frac{\partial^2 \psi}{\partial v^2} = 0, \tag{10}$$

where $\psi(x, z)$ is the poloidal magnetic flux function, x is the radial coordinate relative to the position r_0, and v is the vertical coordinate relative to the position z_0. The coordinates (r_0, z_0) can be chosen arbitrarily subject to the constraint that this point lies close to the X-point. The flux function is related to the radial, B_r, and vertical, B_z, components of the magnetic field through the following relations,

$$B_r = -\frac{1}{r_0 + x}\frac{\partial \psi}{\partial v}, \tag{11a}$$
$$B_z = \frac{1}{r_0 + x}\frac{\partial \psi}{\partial x}. \tag{11b}$$

In (10), we have assumed that the current density in the divertor region is small and therefore can be neglected. As shown in [46] for the case of a second-order null, finite current density effects can be included in the derivation if desired. However, we have found that the simplifying assumption of zero toroidal current provides an adequate model for controller design. Indeed, as will be shown in Section 4, closed-loop simulations suggest that a controller based upon (10) can achieve many desired SFD configurations on NSTX–U.

We next expand the flux function as a series to second-order,

$$\psi(x, v) = l_1 x + l_2 v + q_1 x^2 + 2q_2 xv + q_3 v^2, \tag{12}$$

where we have neglected the constant term as it does not contribute to the components of the poloidal field. Upon substituting (12) into (10) and equating the constant term to zero, we obtain one constraint on the expansion coefficients that must be satisfied for any field configuration,

$$l_1 = 2r_0(q_1 + q_3). \tag{13}$$

Furthermore, by substituting (12) into (11a) and (11b) and employing (13) to eliminate the l_1 coefficient, we obtain formulas for the poloidal field components B_r and B_z,

$$B_r = -\frac{1}{r_0 + x}(l_2 + 2q_2 x + 2q_3 v), \tag{14a}$$
$$B_z = \frac{1}{r_0 + x}(2(r_0 + x)q_1 + 2q_2 v + 2q_3 r_0), \tag{14b}$$

which are linear functions of the l_2, q_1, q_2, q_3 series coefficients. These coefficients can be determined provided that

the values of B_r and B_z at two points in the vicinity of the X-point are known. During plasma operations, the magnetic field values can typically be obtained from a real-time equilibrium reconstruction algorithm.

After computing the expansion coefficients, we may calculate the (r, z) coordinates of the X-point by setting $B_r = B_z = 0$ and solving the resulting equations for the radial and vertical coordinates. We obtain the following,

$$r_x = r_0 + \frac{l_2 q_2 - l_1 q_3}{2\left(q_1 q_3 - q_2^2\right)}, \tag{15a}$$

$$z_x = z_0 + \frac{l_2 q_1 - l_1 q_2}{2\left(q_2^2 - q_1 q_3\right)}. \tag{15b}$$

The X-point coordinates (15a) and (15b) can be easily differentiated to determine the desired response of the X-point position to changes in the poloidal field. Differentiating with the chain rule results in the following,

$$\partial_{\mathbf{B}} r_x = \partial_{\mathbf{c}} r_x \cdot \partial_{\mathbf{B}} \mathbf{c}, \tag{16a}$$

$$\partial_{\mathbf{B}} z_x = \partial_{\mathbf{c}} z_x \cdot \partial_{\mathbf{B}} \mathbf{c}, \tag{16b}$$

where the operator $\partial_{\mathbf{c}}$ denotes partial differentiation with respect to the expansion coefficients. The terms $\partial_{\mathbf{c}} r_x$ and $\partial_{\mathbf{c}} z_x$ are computed directly from (15a) and (15b), while $\partial_{\mathbf{B}} \mathbf{c}$ is the inverse of the matrix that was used to compute the expansion coefficients from the field measurements.

In order to obtain the response of the SFD configuration to changes in the poloidal magnetic field, we first compute the individual response of each X-point, located at the coordinates (r_{x_1}, z_{x_1}) and (r_{x_2}, z_{x_2}), respectively. The responses of the snowflake shape descriptors, as required in (9a) through (9d), are then computed as follows,

$$\partial_{\mathbf{B}} r_c = \left(\partial_{\mathbf{c}} r_{x_1} + \partial_{\mathbf{c}} r_{x_2}\right)/2, \tag{17a}$$

$$\partial_{\mathbf{B}} z_c = \left(\partial_{\mathbf{c}} z_{x_1} + \partial_{\mathbf{c}} z_{x_2}\right)/2, \tag{17b}$$

$$\partial_{\mathbf{B}} d\mathrm{R} = \left(\partial_{\mathbf{c}} r_{x_1} - \partial_{\mathbf{c}} r_{x_2}\right)/2, \tag{17c}$$

$$\partial_{\mathbf{B}} d\mathrm{Z} = \left(\partial_{\mathbf{c}} z_{x_1} - \partial_{\mathbf{c}} z_{x_2}\right)/2. \tag{17d}$$

2.3. Plasma response modeling

The remaining task in the SFD modeling procedure is to compute the derivatives that quantify the linear response of flux and field to changes in the distribution of toroidal plasma current. In particular, we require the matrix $\partial_{\mathbf{I_c}} \boldsymbol{\Psi}_{\mathbf{cp}}$ in (3) as well as the terms $\partial_{\mathbf{J}} \mathbf{B}$ and $\partial_{\mathbf{I_c}} \mathbf{J}$ in (9a) through (9d). The approach that is taken to obtaining these derivatives can be better understood by first decomposing $\partial_{\mathbf{I_c}} \boldsymbol{\Psi}_{\mathbf{cp}}$ as follows,

$$\frac{\partial \boldsymbol{\Psi}_{\mathbf{cp}}}{\partial \mathbf{I_c}} = \frac{\partial \boldsymbol{\Psi}_{\mathbf{cp}}}{\partial \boldsymbol{\xi}_r} \frac{\partial \boldsymbol{\xi}_r}{\partial \mathbf{I_c}} + \frac{\partial \boldsymbol{\Psi}_{\mathbf{cp}}}{\partial \boldsymbol{\xi}_z} \frac{\partial \boldsymbol{\xi}_z}{\partial \mathbf{I_c}}, \tag{18}$$

where $\boldsymbol{\xi}_r$ and $\boldsymbol{\xi}_z$ are plasma fluid element displacement vectors in the radial and vertical directions, respectively. The evaluation of the required derivatives therefore necessitates the calculation of $\partial_{\mathbf{I_c}} \boldsymbol{\xi}_r$ and $\partial_{\mathbf{I_c}} \boldsymbol{\xi}_z$, the response of the plasma fluid elements to changes in the coil currents.

One of two modeling formalisms is typically employed for this purpose: (1) Under the rigid plasma assumption, the plasma current distribution is constrained to move rigidly in the radial and vertical directions such that the relative distribution of plasma current in the poloidal plane remains constant. The response of the plasma is therefore completely defined by the responses of r_C and z_C, the radial and vertical coordinates of the plasma current centroid (not to be confused with r_c and z_c, the coordinates of the SFD centroid). (2) In contrast to the rigid plasma constraint, the plasma fluid elements may be allowed to move independently in both the radial and vertical directions. The total plasma response is therefore determined by the individual displacements of all fluid elements. This response model is often referred to as the nonrigid or perturbed equilibrium model as the model requires the solution of a perturbed form of the Grad-Shafranov equation. It should be emphasized that, in both the rigid and nonrigid models, the assumption is made that all plasma displacements occur in a manner that conserves either a global or local form of force-balance. Further discussion of both rigid [40, 45] and nonrigid [47, 48] response models can be found in the relevant literature.

For SFD control development, we choose to model the plasma as a rigid body due to the relative simplicity of this approach. Our problem is therefore reduced from the calculation of $\partial_{\mathbf{I_c}} \boldsymbol{\xi}_r$ and $\partial_{\mathbf{I_c}} \boldsymbol{\xi}_z$ to the calculation of $\partial_{\mathbf{I_c}} r_C$ and $\partial_{\mathbf{I_c}} z_C$. The response matrices are then used to construct the remaining unknown derivatives in (3) and (9a) through (9d). For details of this procedure, the reader may refer to the appendix.

3. Controller design for the SFD

In this section, we use the linear model developed in Section 2 to design a feedback controller for the SFD configuration on NSTX–U. The resulting control algorithm is constructed from three primary components: (1) a feedforward gain matrix, which is used to estimate the PF coil voltages and currents required to achieve the desired SFD configuration, (2) a full-state feedback control law, which generates a set of voltage commands for the PF coils that is proportional to the error between the target and present values of the coil currents, and (3) an integral feedback term, which improves tracking of the target SFD configuration in the presence of modeling uncertainties and system disturbances by minimizing the integrated error between the desired and present values of the snowflake shape parameters. In Section 3.1, we provide an overview of the control scheme and derive the control law that is used for generating appropriate voltage commands for the PF coils. In Section 3.2, we compute feedback gains for the control system using a standard control design technique known as the linear quadratic regulator. Finally, in Section 3.3, we describe how the state feedback control scheme can be augmented with integral action to ensure proper tracking of the target snowflake configuration. A block diagram

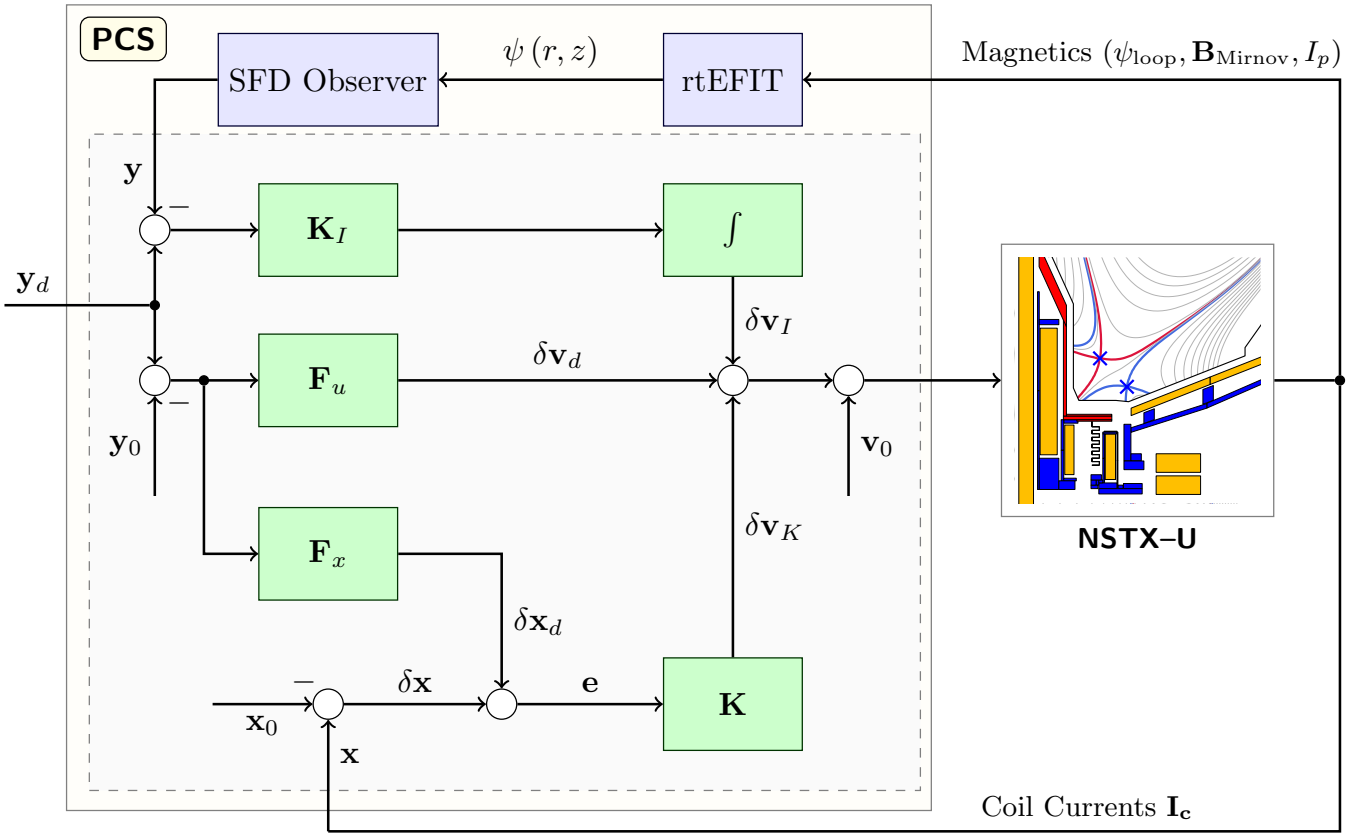

Figure 3: Block diagram depicting the data flow through the snowflake divertor (SFD) control system on NSTX–U. The large yellow rectangle encloses the blocks which represent the components of the SFD control within the Plasma Control System (PCS), namely, the control law (green), the SFD shape observer, and the rtEFIT algorithm for real-time equilibrium reconstruction. The smaller gray rectangle contains blocks representing the subcomponents of the control law as described in this paper, namely, the feedforward term with gain matrices $\mathbf{F}_u$ and $\mathbf{F}_x$, the state-feedback control law for obtaining the desired PF coil currents with optimal gain matrix $\mathbf{K}$ computed by the linear quadratic regulator algorithm, and the integral term with gain matrix $\mathbf{K}_I$ for achieving zero steady-state error in the snowflake shape descriptors.

illustrating the major components of the control system and their interconnections is provided in Figure 3.

3.1. State feedback with reference tracking

The objective of the control algorithm is to command the system to a desired state vector $\mathbf{x}_d$ that corresponds to a set of desired system outputs $\mathbf{y}_d$. In the particular case of the SFD, the desired states are the coil currents and the desired outputs are a set of shape parameters which define the desired SFD configuration. The goal of the control algorithm should therefore be to minimize the state error $\mathbf{e} = \mathbf{x} - \mathbf{x}_d$, the difference between the present and desired values of the state vector (coil currents). Using (1a), the error dynamics can be computed as,

$$\dot{\mathbf{e}} = \mathbf{A}(t)\mathbf{e} + \mathbf{B}(t)\mathbf{u}, \tag{19}$$

where $\mathbf{u} = \mathbf{v} - \mathbf{v}_d$, the difference between the present and desired values of the input voltage vector. Using (19), we can then design a state feedback controller of the following form,

$$\mathbf{u} = -\mathbf{K}(t)\mathbf{e}, \tag{20}$$

where $\mathbf{K}$ is a matrix of feedback gains with dimension $m \times n$, where m is the number of inputs and n is the number of states. The product of $\mathbf{K}$ and $\mathbf{e}$ shall therefore produce a set of appropriate voltages $\mathbf{u}$ for the coils which will result in a minimum state error. Using (20), the total input to the system is as follows,

$$\mathbf{v} = \mathbf{K}(t)\,(\mathbf{x}_d - \mathbf{x}) + \mathbf{v}_d. \tag{21}$$

The remaining task is to compute the desired state vector $\mathbf{x}_d$ and the desired input vector $\mathbf{v}_d$, which we shall refer to hereafter as the feedforward state (coil current) and input (voltage) vectors. This is accomplished as follows: When the system reaches a steady-state ($\dot{\mathbf{x}} = 0$), the system output vector $\mathbf{y}$ should equal the desired value $\mathbf{y}_d$. Using (1a) and (1b), the following conditions are therefore satisfied,

$$0 = \mathbf{A}(t)\mathbf{x}_d + \mathbf{B}(t)\mathbf{v}_d, \tag{22a}$$

$$\mathbf{y}_d = \mathbf{C}(t)\mathbf{x}_d. \tag{22b}$$

Upon solving (22a) and (22b), we obtain,

$$\mathbf{x}_d = \mathbf{C}^\dagger(t)\,\mathbf{y}_d, \tag{23a}$$
$$\mathbf{v}_d = -\mathbf{B}^{-1}(t)\mathbf{A}(t)\mathbf{C}^\dagger(t)\,\mathbf{y}_d, \tag{23b}$$

where the symbol † denotes the matrix pseudoinverse. The expressions (23a) and (23b) are then used to define the following feedforward gain matrices,

$$\mathbf{F}_x = \mathbf{C}^\dagger(t), \tag{24a}$$
$$\mathbf{F}_u = -\mathbf{B}^{-1}(t)\mathbf{A}(t)\mathbf{C}^\dagger(t), \tag{24b}$$

where $\mathbf{F}_x$ is the feedforward state matrix and $\mathbf{F}_u$ is the feedforward input matrix.

Since the linearized model (1a) and (1b) is only valid for small perturbations about the defining equilibrium, it should be emphasized that all vector quantities in this section are measured relative to their equilibrium values. The inputs and outputs to the control algorithm must therefore be expressed in the perturbed coordinate system by addition or subtraction of the corresponding equilibrium quantities. For the sake of simplicity, we have refrained from expressing (19) through (24b) in perturbed coordinates. However, the required coordinate system shifts are depicted explicitly in Figure 3, where $(\mathbf{v}_0, \mathbf{x}_0, \mathbf{y}_0)$ are the equilibrium values of the input, state, and output vectors, respectively. As the model (1a) and (1b) is time-varying, we also note that the control system parameters, such as the feedforward and feedback gain matrices, should be updated periodically to account for changes in the system dynamics, as will be done in Section 4.

3.2. LQR optimal control design

The control law as formulated in (20) and (21) requires that a matrix of feedback control gains $\mathbf{K}$ be computed which converts a vector of state errors to a vector of coil voltage commands. For this purpose, we employ a common technique in control system design known as the linear quadratic regulator (LQR). The algorithm computes a matrix of feedback gains $\mathbf{K}$ which minimizes the following quadratic cost function,

$$\mathcal{J} = \int_0^\infty \left(\mathbf{e}^\mathsf{T}\mathbf{Q}\mathbf{e} + \mathbf{u}^\mathsf{T}\mathbf{R}\mathbf{u}\right) \mathrm{d}t, \tag{25}$$

where $\mathbf{e}$ and $\mathbf{u}$ are the error and input vectors, respectively, as defined in the previous section, and $\mathbf{Q}$ and $\mathbf{R}$ are symmetric, positive-definite weighting matrices with entries that are defined by the control designer. It can be shown that the optimal gain matrix $\mathbf{K}$ which minimizes (25) is given by,

$$\mathbf{K} = \mathbf{R}^{-1}\mathbf{B}^\mathsf{T}\mathbf{P}, \tag{26}$$

where $\mathbf{P}$ is a symmetric, positive-definite matrix that satisfies the matrix equation,

$$\mathbf{A}^\mathsf{T}\mathbf{P} + \mathbf{P}\mathbf{A} - \mathbf{P}\mathbf{B}\mathbf{R}^{-1}\mathbf{B}^\mathsf{T}\mathbf{P} + \mathbf{Q} = 0. \tag{27}$$

This equation is known as the algebraic Riccati equation and is solved iteratively using standard algorithms in commercial software packages such as MATLAB. More details pertaining to state feedback control design and the LQR algorithm may be found in standard reference works [38, 49, 50].

3.3. Integral action

It is well known that the control system as formulated by the feedback law (21) will often perform poorly when attempting to track nonzero reference trajectories for the system outputs. The source of this deficiency is the absence of a term in (21) that is dependent upon the errors between the measured and desired outputs. Rather, output tracking is accomplished indirectly by computing the feedforward currents and voltages in (23a) and (23b) at which the system outputs assume their desired values. This approach therefore requires a highly accurate model of the system dynamics and is unable to compensate for modeling uncertainties or system disturbances. A commonly-employed remedy is to augment the system state vector with a term that depends explicitly on the output tracking errors [51]. In particular, we may introduce a new state $\mathbf{z}$, which is defined as the integral of the error between the desired and measured system outputs,

$$\mathbf{z} = \int_0^t (\mathbf{y}_d - \mathbf{y})\,\mathrm{d}\tau. \tag{28}$$

The dynamics for the augmented system are as follows,

$$\frac{\mathrm{d}}{\mathrm{d}t}\begin{bmatrix}\mathbf{x}\\ \mathbf{z}\end{bmatrix} = \begin{bmatrix}\mathbf{A}(t) & 0\\ -\mathbf{C}(t) & 0\end{bmatrix}\begin{bmatrix}\mathbf{x}\\ \mathbf{z}\end{bmatrix} + \begin{bmatrix}\mathbf{B}(t)\\ 0\end{bmatrix}\mathbf{v} + \begin{bmatrix}0\\ \mathbf{I}\end{bmatrix}\mathbf{y}_d, \tag{29}$$

where $\mathbf{I}$ is the identity matrix. The feedback control law for the augmented system can therefore be expressed as,

$$\mathbf{v} = \mathbf{K}(t)\,(\mathbf{x}_d - \mathbf{x}) + \mathbf{K}_I(t)\,\mathbf{z} + \mathbf{v}_d, \tag{30}$$

where $\mathbf{K}$ is the matrix of state feedback gains as computed in Section 3.2 and $\mathbf{K}_I$ is an additional set of gains for the error integrals. We note that, if the closed-loop system is stable, there will exist a steady-state condition at which $\dot{\mathbf{z}} = 0$ and $\mathbf{y} = \mathbf{y}_d$. The use of integral action therefore guarantees zero error in steady-state between the measured and desired values of the system outputs.

The remaining task of the control design is to compute the matrix $\mathbf{K}_I$ of integral gains. For this purpose, the error vector $\mathbf{e}$ in the cost function (25) may be replaced by the augmented error vector $\mathbf{e}^*$, defined as,

$$\mathbf{e}^* = \begin{bmatrix}\mathbf{e}\\ \mathbf{z}\end{bmatrix}. \tag{31}$$

We may then proceed with a standard LQR control design to compute both the state feedback gain matrix $\mathbf{K}$ as well as the integral gain matrix $\mathbf{K}_I$. As inputs to the cost function for the LQR design, we define the weighting matrices

to be $\mathbf{Q} = \mathrm{diag}(10^{-4} \cdot \mathbf{I}_{3\times3}, 10^{10} \cdot \mathbf{I}_{4\times4})$ and $\mathbf{R} = \rho\mathbf{I}_{3\times3}$, where $\rho = 1$ but can be varied if necessary to achieve the desired transient response. The diagonal elements of the matrix $\mathbf{Q}$ were chosen to provide equal weighting in the cost function to a coil current error of 100A and to an instantaneous error of 5 cm in one of the snowflake parameters. The weights were not selected based upon quantitative criteria but were simply found to yield qualitatively-good controller performance during simulations.

3.4. Equilibrium reconstruction and SFD shape observer

We conclude our discussion of the control algorithm by noting that several additional components, while not the focus of this paper, are required by the control system. In particular, the SFD control requires data from the rtEFIT algorithm for real-time equilibrium reconstruction [52] and the SFD shape observer for identifying the instantaneous locations of the two proximate X-points in the snowflake configuration. Both components are depicted in Figure 3. The rtEFIT algorithm, which was used extensively on both NSTX [53] and NSTX–U [54], computes an approximate solution to the plasma force-balance relation that is constrained by measurements of flux, field, and current from a variety of magnetic sensors on the device. In particular, rtEFIT provides a reasonably accurate estimate of the plasma boundary location to enable control of the boundary shape and divertor geometry. The SFD shape observer is designed to operate in series with rtEFIT and employs an algorithm, similar to that derived in Section 2.2, for approximating the field topology in the divertor region given the field measurements (B_r, B_z) at three points. The X-point locations of the SFD can then be found by solving for the (r, z) coordinates at which $B_r = B_z = 0$. The observer was developed as an alternative to the iterative search method which is used by rtEFIT for locating X-points as this search algorithm is currently not capable of simultaneously locating two proximate X-points. Details of the SFD observer may be found in [37].

4. Feedback control simulation results

The performance of the proposed control system for the SFD on NSTX–U was validated through a series of closed-loop simulations during which the controller was used to achieve and transition between a variety of SFD equilibria. The simulation scenarios were designed to study controller performance in a large subset of the SFD equilibrium space to ensure that control system performance remained robust despite the time-varying response of the configuration. In Section 4.1, we describe the nonlinear shape control simulator that was developed for this work. In Section 4.2, we present closed-loop simulation results to illustrate the capabilities of the controller.

4.1. Nonlinear shape control simulator

The design of control algorithms for the axisymmetric shape and divertor configuration on NSTX (prior to the device upgrade) was, for many years, facilitated by the General Atomics suite of MATLAB/Simulink codes known as the Tokamak System Toolbox (TokSys) [55], a collection of software tools which supports electromagnetic analysis, control system design, and tokamak system simulation. TokSys was used on NSTX, for instance, to study vertical stability dynamics [56], construct predictive models of the plasma response to external fields [57], and design multivariable controllers for the plasma boundary shape [58]. TokSys also enabled verification of control algorithm performance using tools such as the simulation server (simserver), which provided capabilities for closed-loop data transfer between the NSTX Plasma Control System (PCS) and NSTX plant model implemented in MATLAB/Simulink. The simserver was used for testing of control algorithms in a predictive environment prior to deployment on NSTX. However, simulations were typically constructed using linearized models of the plasma response and were therefore only valid for the description of scenarios in which the PF coils imposed small perturbations on the plasma boundary shape and X-point locations. As discussed in Section 1, the SFD configuration exhibits a strongly nonlinear response to the PF coils that is unlikely to be accurately approximated by linearized models. In order to enable high fidelity simulations of SFD discharges, therefore, an effort was undertaken to update the TokSys model to reflect the NSTX–U device configuration and to augment the simulation framework with new capabilities for nonlinear evolution of the plasma equilibrium.[1] The resulting control simulator was configured to simultaneously evolve the currents in PF coils based upon a set of feedback-computed voltage commands, calculate induced currents in passive conducting structures, and update the plasma equilibrium by solving the free-boundary Grad-Shafranov problem.

All toroidally-axisymmetric conductors on the device, namely, the PF coils as well as passive elements such as the vacuum vessel and vertical stabilization plates, were modeled in the simulator as inductively-coupled, lumped parameter circuits in a manner analogous to that which was used in Section 2.1 for modeling of the divertor control coils. The relevant equations for the combined system of conductors are as follows,

$$\mathbf{M_{cc}}\dot{\mathbf{I}}_\mathbf{c} + \mathbf{M_{cv}}\dot{\mathbf{I}}_\mathbf{v} + \dot{\boldsymbol{\Psi}}_\mathbf{cp} + \mathbf{R_c}\mathbf{I_c} = \mathbf{V_c}, \tag{32a}$$

$$\mathbf{M_{vc}}\dot{\mathbf{I}}_\mathbf{c} + \mathbf{M_{vv}}\dot{\mathbf{I}}_\mathbf{v} + \dot{\boldsymbol{\Psi}}_\mathbf{vp} + \mathbf{R_v}\mathbf{I_v} = 0, \tag{32b}$$

were (32a) describes the dynamics of the currents in the PF coils and (32b) describes the dynamics of the currents

[1] We note that nonlinear codes for closed-loop simulation of the plasma equilibrium evolution have been used for control development on other devices. For instance, the DINA [59] code, which solves the free-boundary Grad-Shafranov problem together with a system of flux surface-averaged transport equations, was integrated into the TokSys simulation framework for DIII–D [60]. In addition, the CREATE-NL [61] code has been used for many years to develop shape control algorithms for devices such as JET [62].

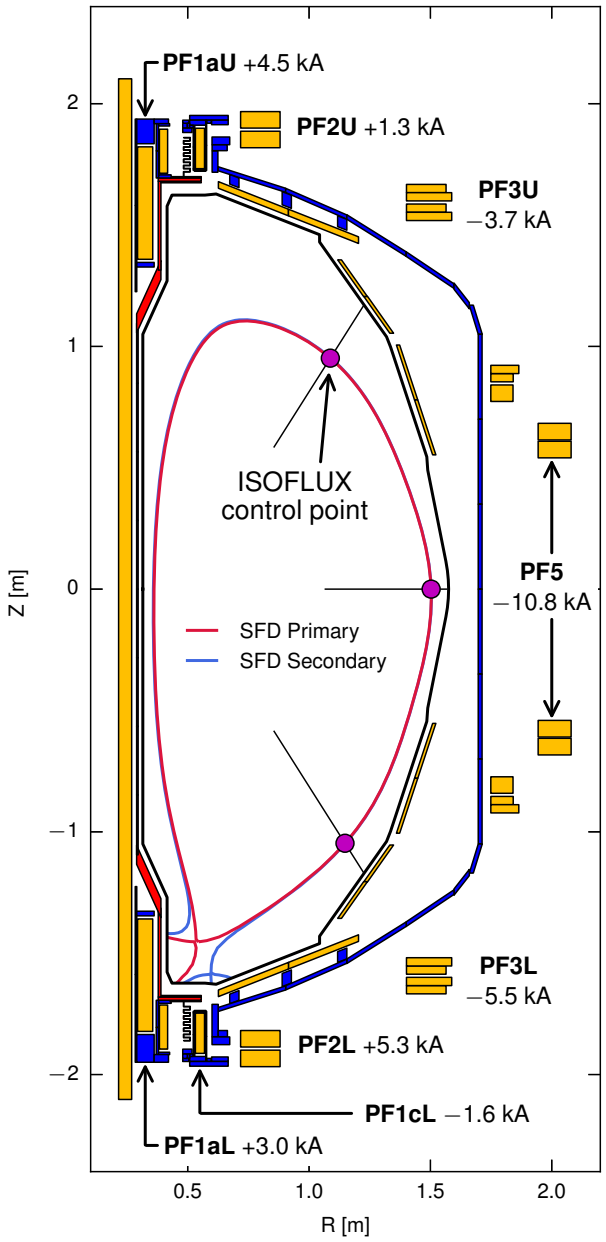

Figure 4: Cross-sectional view of NSTX–U depicting the toroidally-axisymmetric conductors (e.g. poloidal field coils and vacuum vessel) that were modeled in the shape control simulator. Inside the vessel are plotted the primary (red) and secondary (blue) separatrices of the snowflake divertor equilibrium which was used as the initial condition for the closed-loop simulations presented in Section 4.2. Also shown are the coil currents for all active coils in the initial equilibrium and the Isoflux control points which were used to control the plasma boundary shape during simulations.

in the passive conductors. In addition to the terms already defined in Section 2, $\mathbf{M_{cv}}(=\mathbf{M_{vc}}^{\mathsf{T}})$ and $\mathbf{M_{vv}}$ are matrices containing the mutual inductances between coil-passive and passive-passive circuits, respectively, while $\dot{\mathbf{\Psi}}_{\mathbf{vp}}$ represents the change in magnetic flux at the passive conductors due to the plasma response and is computed in the same fashion as $\dot{\mathbf{\Psi}}_{\mathbf{cp}}$ in Section 2. It should be noted that, while the model used for control design in Section 2 only considered the dynamics of the SFD control coils, the coil variables $\mathbf{I_c}$, $\mathbf{R_c}$, and $\mathbf{V_c}$ in (32a) and (32b) contain entries for all active PF coils on the device. In addition to the coil variables, $\mathbf{I_v}$ is a vector containing the currents in the passive circuits, and $\mathbf{R_v}$ is a diagonal matrix containing the resistances of the passive circuits. The resistances of the individual passive conductors were determined by identifying values that produced qualitatively good agreement between model-predicted and measured magnetic diagnostic signals for data obtained during vacuum-only test shots of the PF coils. All other model parameters were computed analytically. Figure 4 provides a cross-sectional view of NSTX–U that depicts the toroidally-axisymmetric conductors which were modeled in the simulator. In total, the circuit model for NSTX–U consisted of 8 circuits for the active PF coils coupled to 40 circuits for the passive conducting structures. We emphasize that the model (32a) and (32b) used for simulation evolves the currents in all PF coils and passive conductors and thereby introduces disturbances for which the SFD control algorithm must compensate. We also note that the system represented by (32a) and (32b) often has one unstable eigenvalue corresponding to the well-known axisymmetric vertical instability. For the purposes of SFD control validation, we artificially stabilized the system by negating the unstable eigenvalue. This procedure is consistent with the assumption that the plasma vertical position is stabilized by a separate control loop (as is done on NSTX–U [54]).

While the conductor currents evolve dynamically in response to applied voltages on the PF coils, the axisymmetric plasma remains in equilibrium on time scales of interest for shape control and therefore satisfies the Grad-Shafranov equation,

$$\Delta^*\psi = -\mu_0 r^2 p' - FF', \tag{33}$$

where $\psi(r,z)$ is the poloidal magnetic flux function, r is the major radius, $p(\psi)$ is the pressure, and $F(\psi) = rB_\phi$, where B_ϕ is the toroidal magnetic field and the prime notation denotes differentiation with respect to ψ. In addition to the equilibrium relation (33), a set of initial-boundary conditions must be supplied to define the profile functions p' and FF' as well as the plasma boundary flux. In the control simulator, (33) was solved using a MATLAB-based free-boundary equilibrium code which is included as part of the TokSys software package. The required inputs to the solver include the instantaneous values of the coil and vessel currents as computed from (32a) and (32b) for determining the applied flux and plasma boundary shape. Also provided as inputs are the scalar parameters I_p, β_p, and l_i for defining the p' and FF' profiles, both of which are modeled as polynomial splines with coefficients that are varied automatically during simulations to approximately conserve the volume-integrated scalar inputs.

As shown in Figure 4, the plasma boundary and divertor configuration were controlled by a total of 8 PF coils

which were operated in closed-loop by one of two algorithms. The voltage commands for the PF1aL, PF1cL, and PF2L coils were computed by the SFD control algorithm as described in this paper, while the remaining PF coils were controlled by the Isoflux algorithm with the aim of maintaining the plasma boundary shape and upper X-point position while the SFD configuration was modified by the lower divertor coils. The Isoflux algorithm, which is the primary shape control algorithm used on NSTX–U [54], is a predominantly single-input-single-output algorithm that regulates the plasma boundary shape by minimizing the errors between the fluxes at several control points on the desired boundary, as shown in Figure 4, and the flux at the boundary-defining X-point. During simulations, the PF3U, PF5, and PF3L coils were allocated for control of the fluxes at the three control points, while the PF2U and PF1aU coils were assigned to directly control the radial and vertical coordinates of the upper X-point, respectively. The voltage commands for all coils under Isoflux control were computed using a PID control law with gains that were tuned empirically during simulations to yield qualitatively good transient response and small steady-state error.

In Figure 5, we provide a flowchart illustrating the major components of the nonlinear shape control simulator and their interconnections. The simulations were initialized using a SFD-minus equilibrium, shown in Figure 4, with $I_p = 1$ MA, $\beta_p = 1.0$, and $l_i = 0.6$ as generated by the free-boundary Grad-Shafranov solver in TokSys. After initialization, the nonlinear simulations proceeded by performing the following sequence of calculations during each simulation time-step: At the start of the time-step, the equilibrium was analyzed by the shape and SFD observer, as described briefly in Section 3.4, to determine the X-point locations and Isoflux control point fluxes. The voltage commands for the PF coils were then computed with the Isoflux and SFD control algorithms based upon the errors between the present and target values of the boundary shape and divertor configuration. Using as input the feedback-computed voltage commands, the circuit model (32a) and (32b) was then integrated to determine the instantaneous currents in all PF coil and passive structure circuits. The free-boundary Grad-Shafranov equation (33) was then solved subject to the constraints imposed by the circuit currents and plasma profiles. The equilibrium flux function, as computed on a 65×65 rectangular grid using the free-boundary solver, was then used as input for the next simulation time-step. This process was repeated until the simulation reached a user-defined stop time.

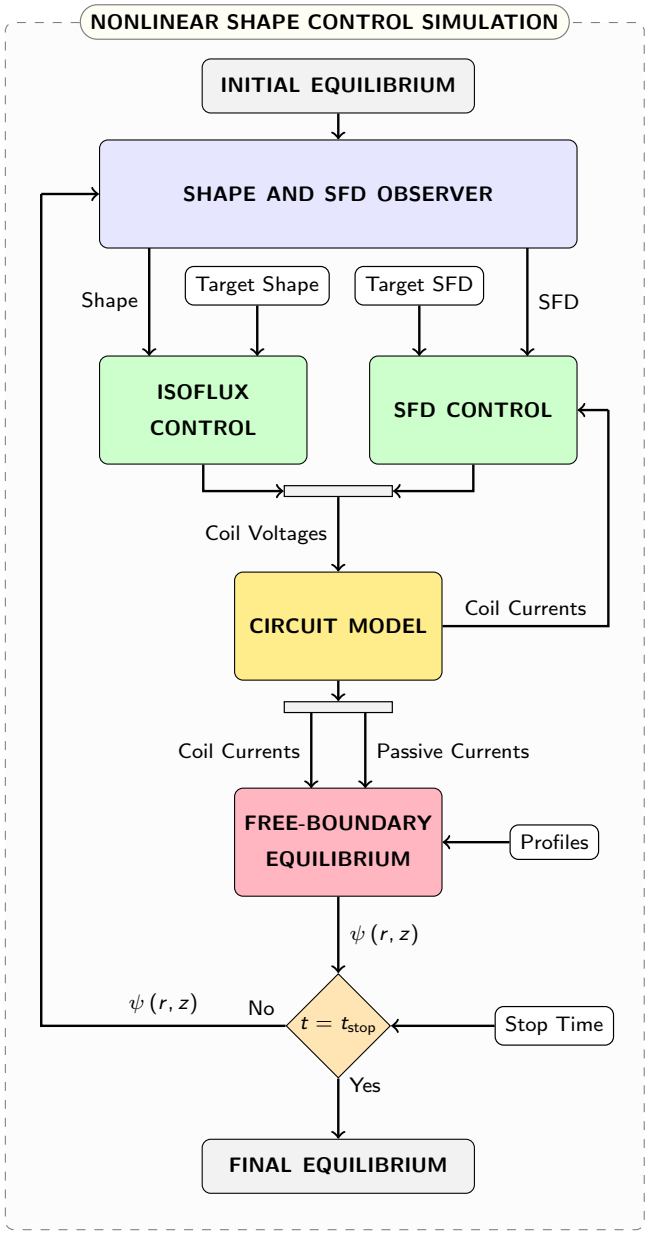

Figure 5: Flowchart depicting the major components of the NSTX–U nonlinear shape control simulator and their interconnections. The white rectangles denote quantities which are defined by the user prior to simulations.

4.2. Simulation results

The nonlinear simulator was used to validate the performance of the SFD control algorithm with particular emphasis on the demonstration of controlled operations in and transitions between a variety of divertor configurations. In particular, we studied controller performance in three scenarios: (a) transition of the configuration from a LFS SFD-minus to a SFD-plus followed by a HFS SFD-minus as achieved by scanning the angular orientation θ of the primary and secondary X-points while maintaining a constant distance ρ between the X-points, (b) scan of the X-point separation distance ρ at constant angular orientation θ in SFD-plus, and (c) scan of the X-point separation distance ρ at constant angular orientation θ in LFS SFD-minus. The simulation scenarios were designed to ensure that control system performance remained robust throughout a large subset of the SFD equilibrium space.

The simulations were configured to run for a duration of 1.2s (Stop Time in Figure 5), a value which was chosen to

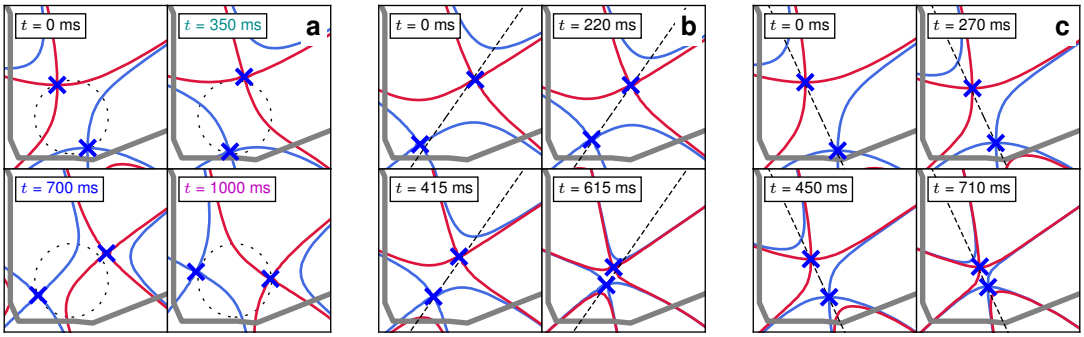

Figure 6: Closed-loop simulation results depicting the primary (red) and secondary (blue) separatrices and their corresponding X-points during controlled scans of the snowflake divertor (SFD) configuration on NSTX–U in three scenarios: (a) transition of the configuration from a low-field-side SFD-minus ($t = 0$ ms) to a SFD-plus ($t = 350$ ms) followed by a high-field-side SFD-minus ($t = 700$ ms and $t = 1000$ ms) which was achieved by scanning the angular orientation θ of the primary and secondary X-points while maintaining a constant distance ρ between the X-points, (b) scan of the X-point separation distance ρ at constant angular orientation θ in SFD-plus, and (c) scan of the X-point separation distance ρ at constant orientation θ in low-field-side SFD-minus. Plotted also are black dashed curves which indicate the target trajectories for the X-points during each scenario.

ensure that adequate time was allotted for making large changes to the divertor configuration without requiring a controller design with an overly-aggressive transient response. In this work, our primary goal was to demonstrate control of the relative positioning of the two X-points, defined by the parameters dR and dZ, as this capability will likely be most important for preliminary NSTX–U operations. To ensure that every requested pair of dR and dZ values could be achieved, it was decided that only three SFD parameters would be actively controlled such that the LTV model (1a) and (1b) becomes fully-invertible (as the number of actuators is then equal to the number of outputs). In this case, we expect that a well-designed controller can achieve any reasonable set of three targets for the SFD parameters, as is observed in the following simulation results. It was determined that the radial coordinate of the centroid r_c required active control to prevent the configuration from impacting the inner wall. This difficulty may arise due to the absence of inner gap control on NSTX–U. The choice was therefore made to control the set of parameters $\{r_c, d\text{R}, d\text{Z}\}$ and allow the centroid vertical coordinate z_c to be a free parameter. While the coordinate z_c is not actively controlled by the SFD algorithm, we note that the vertical position of the divertor configuration is still somewhat constrained by the global boundary shape. Target values for dR and dZ were defined indirectly by first specifying target values for the X-point separation distance ρ and angular orientation θ and then converting the targets to Cartesian format using simple formulas. For the duration of this paper, we refer to dR and dZ as directly-controlled as these parameters appear explicitly in the LTV model (1a) and (1b). The parameters ρ and θ are referred to as indirectly-controlled. We note that the LTV model and corresponding controller gains were updated every 5 ms to account for the evolving equilibrium. This time increment was found to yield an acceptable balance between controller performance and simulation execution time. Furthermore, 5 ms is approximately the time required for performing one cycle of the rtEFIT algorithm for real-time equilibrium reconstruction on NSTX–U [54].

Figure 6 displays a sequence of equilibria for each of the three simulation scenarios. Plotted also are black dashed curves which indicate the target trajectories for the two X-points during each scenario. In Figure 6a, we illustrate the results of the scan of the X-point angular orientation in which the SFD configuration transitions from a LFS SFD-minus ($t = 0$ ms) to a SFD-plus ($t = 350$ ms) followed by a HFS SFD-minus ($t = 700$ ms and $t = 1000$ ms). We observe that the control algorithm is capable of rotating the X-points through a significant angular range while maintaining the X-points at a near-constant separation distance. It appears that, at least in this simulation, the algorithm presented in this paper enables controlled operations in both the LFS SFD-minus and HFS SFD-minus configurations. As we recall, the absence of this capability was a significant shortcoming of prior algorithms. Figures 6b and 6c illustrate the results of the controlled scans of the X-point separation distance in the SFD-plus and LFS SFD-minus configurations, respectively. In each instance, the control algorithm converts the equilibrium from a SFD configuration with separation distance $\rho \approx 20$ cm ($t = 0$ ms) to a near-exact SFD with $\rho \approx 6$ cm ($t = 615$ ms for SFD-plus and $t = 710$ ms for LFS SFD-minus). In each scenario, the angular orientation of the two X-points remains fairly constant throughout the scan. When considered together, the results of the three simulation scenarios suggest that the control algorithm enables operations in a variety of SFD equilibria on NSTX–U despite the challenges imposed by the highly-nonlinear nature of the SFD configuration response.

In Figure 7, we provide time traces of the six SFD shape parameters, as first defined in Section 2, during the scan of

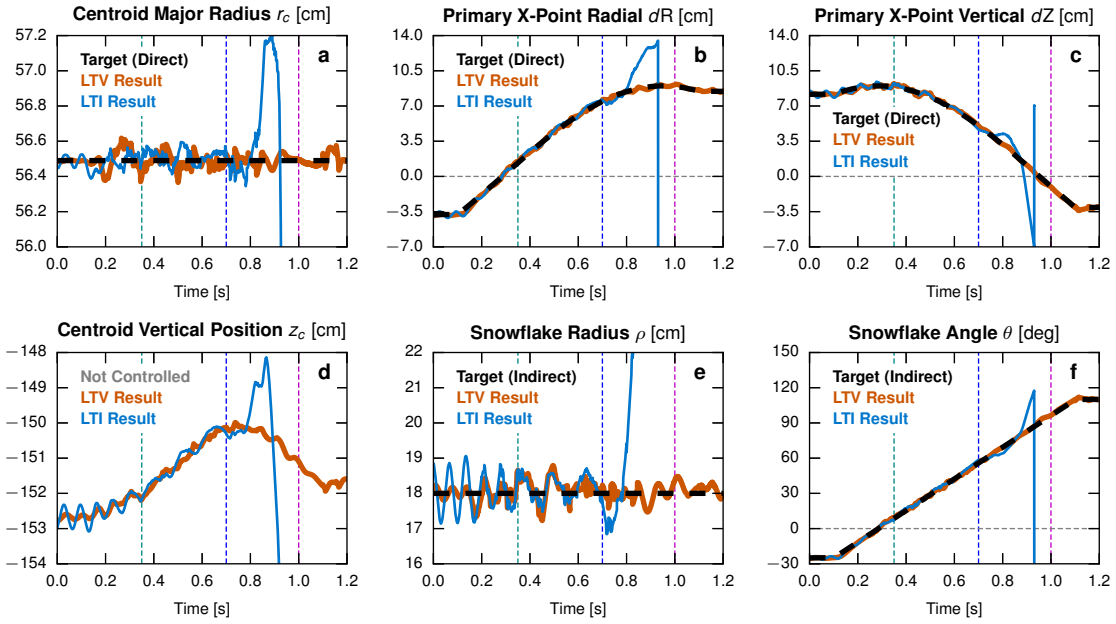

Figure 7: Time series for the six snowflake divertor (SFD) parameters, as defined in Figure 2, during a scan of the configuration from a low-field-side SFD-minus to a SFD-plus followed by a high-field-side SFD-minus. The LTV curves (orange) are the results of a simulation in which the controller gains were updated every 5 ms, while the LTI curves (blue) are the results of a simulation in which the gains were static. Indicated also in black dashes are the target trajectories for the SFD parameters as provided to the control system. The colored dashed lines on each plot indicate the instantaneous values of the parameters for each of the similarly colored equilibria in Figure 6a.

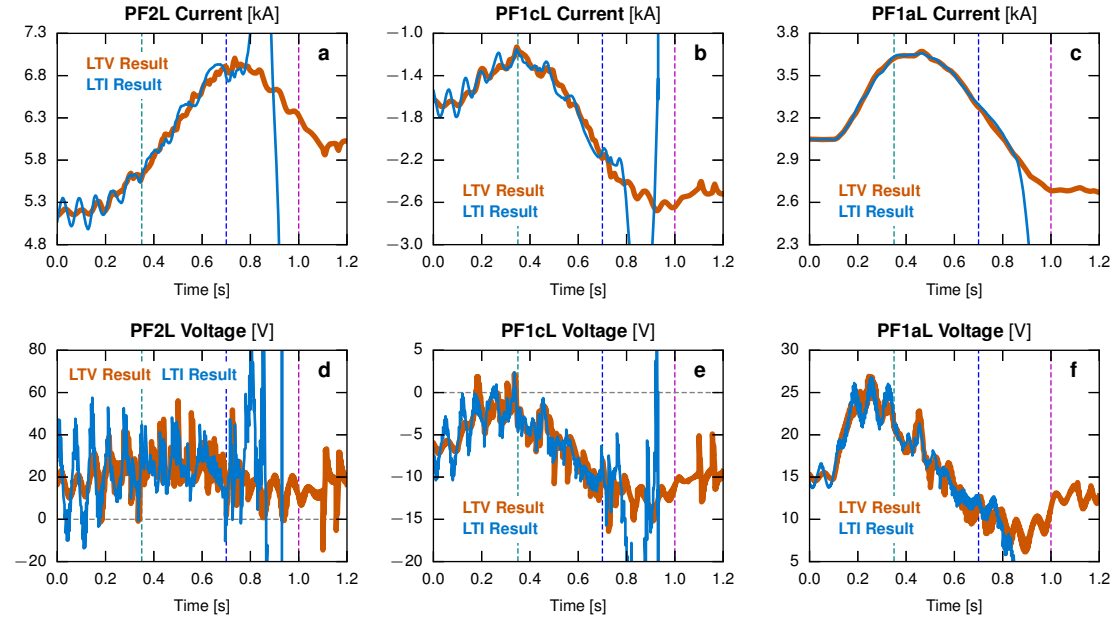

Figure 8: Poloidal field coil currents (a,b,c) and voltages (d,e,f) for the PF2L (a,d), PF1cL (b,e), and PF1aL (c,f) divertor coils during a scan of the snowflake (SFD) configuration from a low-field-side SFD-minus to a SFD-plus followed by a high-field-side SFD-minus. The LTV curves (orange) are the results of a simulation in which the controller gains were updated every 5 ms, while the LTI curves (blue) are the results of a simulation in which the gains were static. The colored dashed lines on each plot indicate the instantaneous values of the currents and voltages for each of the similarly colored equilibria in Figure 6a. Each coil has a different maximum current and available voltage. However, the maximum current and voltage for each of the coils shown are at least 13 kA and 1 kV, respectively.

the X-point angular orientation at constant X-point separation distance, as seen in Figure 6a. Figures 7a through 7c display the directly-controlled parameters, namely, the major radius r_c of the SFD centroid as well as the radial dR and vertical dZ displacements of the primary X-point from the centroid. Figures 7d through 7f display the indirectly-

controlled parameters, namely, the vertical position z_c of the SFD centroid, the X-point separation distance ρ, and the angular orientation θ. For each parameter, we illustrate the time traces from two simulations, one in which the LTV model and controller gains were updated every 5 ms (orange) and one in which the model and controller gains were time-invariant (blue) and computed using the initial equilibrium shown in Figure 4. Furthermore, Figure 8 displays the currents and voltages for the PF2L, PF1cL, and PF1aL divertor coils during simulations using both the time-dependent (orange) and time-invariant (blue) controllers. We emphasize that the PF coil currents and voltages remained well-within their allowable ranges during all simulations. The behavior of the shape parameters, currents, and voltages during the two additional scenarios was similar to that displayed in Figures 7 and 8. This data is therefore not shown for the sake of brevity.

As seen in Figures 7 and 8, there is a noticeable discrepancy between the performance of the time-dependent (orange) and time-invariant (blue) controllers during the scan of the angular orientation of the two X-points. Indeed, we observe that, when $t \approx 800$ ms and $\theta \approx 90°$, the performance of the time-invariant controller deteriorates significantly, ultimately resulting in the abrupt loss of control over all SFD shape parameters. On the contrary, the time-dependent controller, for which the model and controller gains were updated every 5 ms, yields excellent closed-loop tracking of the time-dependent target trajectories for all parameters. As we alluded to at the beginning of Section 2, the simulation results demonstrate that an LTV controller which can properly account for the time-evolving response of the SFD configuration is not only desirable but necessary for achieving acceptable controller performance. We note that the performance discrepancy between the time-dependent and time-invariant controllers was only manifested in the nonlinear simulations and was not encountered when linear response models were used in place of the free-boundary equilibrium solver. The simulation results therefore justify the efforts that were made for this paper to develop a model-based LTV control algorithm for the SFD configuration and the nonlinear shape control simulator that is required for proper controller validation.

5. Conclusion

In this paper, we have presented the design and simulation of a feedback control algorithm for SFD configurations on NSTX–U. A model of the SFD response to applied voltages on the divertor control coils was derived and then used, in conjunction with multivariable control techniques, to design an optimal feedback controller for the configuration. The model-based nature of the controller design ensures that model parameters and controller gains may be updated periodically to account for the time-evolving dynamical response of the configuration – a significant improvement over prior control schemes. In order to enable high fidelity simulations of SFD discharges, a nonlinear simulator for axisymmetric shape control was developed for NSTX–U which simultaneously evolves the currents in PF coils based upon a set of feedback-computed voltage commands, calculates the induced currents in passive conducting structures, and updates the plasma equilibrium by solving the free-boundary Grad-Shafranov problem. Simulation results suggest that a time-varying controller which can properly account for the evolving SFD dynamical response is not only desirable but necessary for achieving acceptable controller performance. The algorithm presented in this paper has been implemented in the NSTX–U PCS in preparation for future control and divertor physics experiments.

Future control development efforts on NSTX–U will proceed along several avenues: For the development of improved control algorithms for advanced divertor configurations, near-term work will focus on augmenting the SFD algorithm to enable control of additional divertor parameters. For instance, the control-oriented model which was developed in Section 2 may be extended to include the response of the strike point position(s), as simultaneous control of two X-points and the strike point location is required for configurations such as the X-divertor. Additional parameters of relevance to NSTX–U divertor operations include the poloidal flux expansion as well as field line angle-of-incidence. In addition to algorithm development, additional features, such as power supply dynamics and control system latency, can be added to the nonlinear control simulator as presented in Section 4 to increase simulation fidelity. Finally, we note that the control development framework for the SFD may be applied to other tokamak systems in which system nonlinearities or actuator coupling may be relevant. Future work at NSTX–U will include integration of the SFD controller into a model-based algorithm for control of the full plasma boundary as well as the development of time-dependent controllers for the plasma shape during the current ramp-up.

Acknowledgments

This research was supported by the United States Department of Defense (DoD) through the National Defense Science & Engineering Graduate Fellowship (NDSEG) program as well as by the United States Department of Energy (DoE) under contract number DE-AC02-09CH11466.

Notes: The digital data for this publication can be found in: https://dataspace.princeton.edu/jspui/handle/88435/dsp01j6731612k.

Notice: This manuscript is based upon work supported by the United States Department of Energy, Office of Science, Office of Fusion Energy Sciences, and has been authored by Princeton University under contract number DE-AC02-09CH11466 with the United States Department

Appendix

In this appendix, we derive the rigid plasma response model that is used in Section 2 to develop a linearized model of the SFD configuration response. As stated in the main text, under the rigid plasma assumption, the plasma current distribution is constrained to move rigidly in the radial and vertical directions such that the relative distribution of plasma current in the poloidal plane remains constant. The response of the plasma is therefore completely defined by the responses of r_C and z_C, the radial and vertical coordinates of the plasma current centroid. The response of the centroid position to changes in the conductor currents can be decomposed as follows,

$$\frac{\partial r_C}{\partial \mathbf{I}} = \frac{\partial F_r}{\partial \mathbf{I}} \left(\frac{\partial F_r}{\partial r_C} \right)^{-1}, \tag{34a}$$

$$\frac{\partial z_C}{\partial \mathbf{I}} = \frac{\partial F_z}{\partial \mathbf{I}} \left(\frac{\partial F_z}{\partial z_C} \right)^{-1}, \tag{34b}$$

where $\mathbf{I}$ is a vector of (perturbed) conductor currents and F_r and F_z are the total radial and vertical forces on the plasma, respectively. Under the rigid plasma assumption, the radial and vertical forces can be expressed as follows,

$$F_r = \int \left(\mathbf{J} \times \mathbf{B}_{\text{vac}} \right)_r \, \mathrm{d}V + \frac{\mu_0 I_p^2}{2} \left(\ln \frac{8R}{a\sqrt{\kappa}} + \beta_p + \frac{l_i}{2} - \frac{3}{2} \right), \tag{35a}$$

$$F_z = \int \left(\mathbf{J} \times \mathbf{B}_{\text{vac}} \right)_z \, \mathrm{d}V, \tag{35b}$$

where $\mathbf{B}_{\text{vac}}$ is the magnetic field generated by the conductors and the subscripts r and z denote projections of the Lorentz force in the radial and vertical directions, respectively. The second term in (35a) is an approximation for the outward radial force on the plasma and is a function of the plasma current I_p, major radius R, minor radius a, elongation κ, poloidal beta β_p, and normalized inductance l_i [63].

The derivatives which are required for computing the responses of r_C and z_C can be computed directly from (35a) and (35b). For the responses of the forces with respect to changes in the conductor currents, we obtain,

$$\frac{\partial F_r}{\partial \mathbf{I}} = \int J_\phi \frac{\partial M_{pc}}{\partial r} \, \mathrm{d}r \, \mathrm{d}z, \tag{36a}$$

$$\frac{\partial F_z}{\partial \mathbf{I}} = \int J_\phi \frac{\partial M_{pc}}{\partial z} \, \mathrm{d}r \, \mathrm{d}z, \tag{36b}$$

where J_ϕ is the toroidal component of the plasma current density and M_{pc} is the vacuum mutual inductance between the plasma and the conductors. Furthermore, for the responses of the forces with respect to changes in the centroid position, we find,

$$\frac{\partial F_r}{\partial r_C} = 2\pi \int r \frac{\partial J_\phi}{\partial r_C} B_{z\text{vac}} \, \mathrm{d}r \, \mathrm{d}z + \frac{\mu_0 I_p^2}{2 r_C}, \tag{37a}$$

$$\frac{\partial F_z}{\partial z_C} = -2\pi \int r \frac{\partial J_\phi}{\partial z_C} B_{r\text{vac}} \, \mathrm{d}r \, \mathrm{d}z, \tag{37b}$$

where $B_{r\text{vac}}$ and $B_{z\text{vac}}$ are the radial and vertical components of the vacuum magnetic field, respectively. The expressions in (37a) and (37b) can be further simplified through use of the identities $\partial_{r_C} J_\phi = -\partial_r J_\phi$ and $\partial_{z_C} J_\phi = -\partial_z J_\phi$.

The derivatives which are required for the model in Section 2 may now be computed directly from (34a) through (37b). The response of the plasma current distribution to changes in the conductor currents is computed as,

$$\frac{\partial \mathbf{J}}{\partial \mathbf{I}} = \frac{\partial J_\phi}{\partial r_C} \frac{\partial r_C}{\partial \mathbf{I}} + \frac{\partial J_\phi}{\partial z_C} \frac{\partial z_C}{\partial \mathbf{I}}, \tag{38}$$

while the response of the plasma flux the changes in the conductor currents is,

$$\frac{\partial \boldsymbol{\Psi}_{\mathbf{cp}}}{\partial \mathbf{I}} = M_{cp} \left(\frac{\partial J_\phi}{\partial r_C} \frac{\partial r_C}{\partial \mathbf{I}} + \frac{\partial J_\phi}{\partial z_C} \frac{\partial z_C}{\partial \mathbf{I}} \right). \tag{39}$$

References

[1] MENARD, J. E., GERHARDT, S., BELL, M., et al., Nuclear Fusion **52** (2012), doi:10.1088/0029-5515/52/8/083015.

[2] MENARD, J. E., ALLAIN, J. P., BATTAGLIA, D. J., et al., Nuclear Fusion **57** (2017), doi:10.1088/1741-4326/aa600a.

[3] BATTAGLIA, D. J., BOYER, M. D., GERHARDT, S., et al., Nuclear Fusion **58** (2018), doi:10.1088/1741-4326/aaa6e0.

[4] GOLDSTON, R. J., MENARD, J. E., ALLAIN, J. P., et al., An Experiment to Tame the Plasma Material Interface FT/P3-12, in *Proceedings of the 22nd International Conference on Fusion Energy*, IAEA, Geneva, Switzerland, 2008.

[5] STAMBAUGH, R. D., CHAN, V. S., GAROFALO, A. M., et al., Fusion Science and Technology **59** (2011), doi:10.13182/FST59-279.

[6] MENARD, J. E., BROWN, T., EL-GUEBALY, L., et al., Nuclear Fusion **56** (2016), doi:10.1088/0029-5515/56/10/106023.

[7] ONO, M., KAYE, S. M., PENG, Y.-K., et al., Nuclear Fusion **40** (2000), doi:10.1088/0029-5515/40/3Y/316.

[8] SYKES, A., AKERS, R. J., APPEL, L. C., et al., Nuclear Fusion **41** (2001), doi:10.1088/0029-5515/41/10/310.

[9] KAYE, S. M., BELL, R. E., GATES, D., et al., Physical Review Letters **98** (2007), doi:10.1103/PhysRevLett.98.175002.

[10] PODESTÀ, M., HEIDBRINK, W. W., LIU, D., et al., Physics of Plasmas **16** (2009), doi:10.1063/1.3080724.

[11] GERHARDT, S. P., GATES, D. A., KAYE, S. M., et al., Nuclear Fusion **51** (2011), doi:10.1088/0029-5515/51/7/073031.

[12] MENARD, J. E., GERHARDT, S. P., MYERS, C. E., et al., Power exhaust scenarios & control for projected high-power NSTX-U operation, in *Proceedings of the 59th Annual Meeting of the APS Division of Plasma Physics*, American Physical Society, Milwaukee, WI, 2017.

[13] EICH, T., SIEGLIN, B., SCARABOSIO, A., et al., Physical Review Letters **107** (2011), doi:10.1103/PhysRevLett.107.215001.

[14] GRAY, T. K., MAINGI, R., SOUKHANOVSKII, V. A., et al., Journal of Nuclear Materials **415** (2011), doi:10.1016/j.jnucmat.2011.01.029.

[15] EICH, T., LEONARD, A. W., PITTS, R. A., et al., Nuclear Fusion **53** (2013), doi:10.1088/0029-5515/53/9/093031.

[16] THORNTON, A. J., KIRK, A., and the MAST Team, Plasma Physics and Controlled Fusion **56** (2014), doi:10.1088/0741-3335/56/5/055008.

[17] RYUTOV, D. D., Physics of Plasmas **14** (2007), doi:10.1063/1.2738399.

[18] KOTSCHENREUTHER, M., VALANJU, P., COVELE, B., and MAHAJAN, S., Physics of Plasmas **20** (2013), doi:10.1063/1.4824735.

[19] VALANJU, P. M., KOTSCHENREUTHER, M., MAHAJAN, S. M., and CANIK, J., Physics of Plasmas **16** (2009), doi:10.1063/1.3110984.

[20] LABOMBARD, B., Bulletin of the American Physical Society **58** (2014).

[21] RYUTOV, D. D. and SOUKHANOVSKII, V. A., Physics of Plasmas **22** (2015), doi:10.1063/1.4935115.

[22] PIRAS, F., CODA, S., DUVAL, B. P., et al., Nuclear Fusion **52** (2010), doi:10.1088/0741-3335/52/12/124010.

[23] REIMERDES, H., CANAL, G. P., DUVAL, B. P., et al., Plasma Physics and Controlled Fusion **55** (2013), doi:10.1088/0741-3335/55/12/124027.

[24] VIJVERS, W. A. J., CANAL, G. P., LABIT, B., et al., Nuclear Fusion **54** (2014), doi:10.1088/0029-5515/54/2/023009.

[25] CANAL, G. P., LUNT, T., REIMERDES, H., et al., Nuclear Fusion **55** (2015), doi:10.1088/0029-5515/55/12/123023.

[26] SOUKHANOVSKII, V. A., AHN, J.-W., BELL, R. E., et al., Nuclear Fusion **51** (2011), doi:10.1088/0029-5515/51/1/012001.

[27] SOUKHANOVSKII, V. A., BELL, R. E., DIALLO, A., et al., Physics of Plasmas **19** (2012), doi:10.1063/1.4737117.

[28] CALABRÒ, G., XIAO, B. J., CHEN, S. L., et al., Nuclear Fusion **55** (2015), doi:10.1088/0029-5515/55/8/083005.

[29] SOUKHANOVSKII, V. A., ALLEN, S. L., FENSTERMACHER, M. E., et al., Nuclear Fusion **58** (2018), doi:10.1088/1741-4326/aaa6de.

[30] HUANG, J. and MENARD, J., Journal of Undergraduate Research **6** (2006).

[31] SOUKHANOVSKII, V. A., ALLEN, S. L., FENSTERMACHER, M. E., et al., IEEE Transactions on Plasma Science **44** (2016), doi:10.1109/TPS.2016.2625325.

[32] ROGNLIEN, T. D., MILOVICH, J. L., RENSINK, M. E., and PORTER, G. D., Journal of Nuclear Materials **196-198** (1992), doi:10.1016/S0022-3115(06)80058-9.

[33] MEIER, E. T., GERHARDT, S., MENARD, J. E., ROGNLIEN, T. D., and SOUKHANOVSKII, V. A., Nuclear Fusion **55** (2015), doi:10.1088/0029-5515/55/8/086002.

[34] LACKNER, K. and ZOHM, H., Fusion Science and Technology **63** (2013), doi:10.13182/FST12-520.

[35] ASAKURA, N., SHINYA, K., TOBITA, K., et al., Fusion Science and Technology **63** (2013), doi:10.13182/FST13-A16876.

[36] KOLEMEN, E., GATES, D. A., ROWLEY, C. W., et al., Nuclear Fusion **50** (2010), doi:10.1088/0029-5515/50/10/105010.

[37] KOLEMEN, E., VAIL, P. J., MAKOWSKI, M. A., et al., Nuclear Fusion **58** (2018), doi:10.1088/1741-4326/aab0d3.

[38] ÅSTRÖM, K. J. and MURRAY, R. M., *Feedback Systems: An Introduction for Scientists and Engineers*, Princeton University Press, 1 edition, 2008.

[39] LEITH, D. J. and LEITHEAD, W. E., International Journal of Control **73** (2000), doi:10.1080/002071700411304.

[40] COUTLIS, A., BANDYOPADHYAY, I., LISTER, J. B., et al., Nuclear Fusion **39** (1999), doi:10.1088/0029-5515/39/5/307.

[41] BOYER, M. D., ANDRE, R., GATES, D. A., et al., Nuclear Fusion **55** (2015), doi:10.1088/0029-5515/55/5/053033.

[42] BOYER, M. D., BARTON, J., SCHUSTER, E., et al., Plasma Physics and Controlled Fusion **55** (2013), doi:10.1088/0741-3335/55/10/105007.

[43] GOUMIRI, I. R., ROWLEY, C. W., SABBAGH, S. A., et al., Nuclear Fusion **56** (2016), doi:10.1088/0029-5515/56/3/036023.

[44] ARIOLA, M. and PIRONTI, A., *Magnetic Control of Tokamak Plasmas*, Springer-Verlag, 2008.

[45] WALKER, M. L. and HUMPHREYS, D. A., Fusion Science and Technology **50** (2006), doi:10.13182/FST06-A1271.

[46] RYUTOV, D. D., MAKOWSKI, M. A., and UMANSKY, M. V., Plasma Physics and Controlled Fusion **52** (2010), doi:10.1088/0741-3335/52/10/105001.

[47] ALBANESE, R. and VILLONE, F., Nuclear Fusion **38** (1998), doi:10.1088/0029-5515/38/5/307.

[48] WELANDER, A. S., DERANIAN, R. D., HUMPHREYS, D. A., LEUER, J. A., and WALKER, M. L., Fusion Science and Technology **47** (2005), doi:10.13182/FST05-A778.

[49] FRIEDLAND, B., *Control System Design: An Introduction to State-Space Methods*, McGraw-Hill Book Company, 1 edition, 1968.

[50] STENGEL, R. F., *Optimal Control and Estimation*, Dover Publications, 1 edition, 1994.

[51] YOUNG, P. C. and WILLEMS, J. C., International Journal of Control **15** (1972), doi:10.1080/00207177208932211.

[52] FERRON, J. R., WALKER, M. L., LAO, L. L., et al., Nuclear Fusion **38** (1998), doi:10.1088/0029-5515/38/7/308.

[53] GATES, D. A., FERRON, J. R., BELL, M., et al., Nuclear Fusion **46** (2006), doi:10.1088/0029-5515/46/1/002.

[54] BOYER, M. D., BATTAGLIA, D. J., MUELLER, D., et al., Nuclear Fusion **58** (2018), doi:10.1088/1741-4326/aaa4d0.

[55] HUMPHREYS, D. A., FERRON, J. R., BAKHTIARI, M., et al., Nuclear Fusion **47** (2007), doi:10.1088/0029-5515/47/8/028.

[56] HUMPHREYS, D. A., CASPER, T. A., EIDIETIS, N., et al., Nuclear Fusion **49** (2009), doi:10.1088/0029-5515/49/11/115003.

[57] WALKER, M. L., HUMPHREYS, D. A., EIDIETIS, N. W., et al., System Modeling, Validation, and Design of Shape Controllers for NSTX, in *Proceedings of the 53rd Annual Meeting of the APS Division of Plasma Physics*, American Physical Society, Salt Lake City, UT, 2011.

[58] SHI, W., ALSARHEED, M., SCHUSTER, E., et al., Fusion Engineering and Design **86** (2011), doi:10.1016/j.fusengdes.2011.03.023.

[59] KHAYRUTDINOV, R. R. and LUKASH, V. E., Journal of Computational Physics **109** (1993), doi:10.1006/jcph.1993.1211.

[60] LEUER, J. A., DERANIAN, R. D., FERRON, J. R., et al., DIII–D Plasma Control Simulation Environment, in *Proceedings of the 20th IEEE/NPSS Symposium on Fusion Engineering*, IEEE, San Diego, CA, 2003.

[61] ALBANESE, R., AMBROSINO, R., and MATTEI, M., Fusion Engineering and Design **96-97** (2015), doi:10.1016/j.fusengdes.2015.06.162.

[62] ALBANESE, R., AMBROSINO, G., ARIOLA, M., et al., Fusion Engineering and Design **74** (2005), doi:10.1016/j.fusengdes.2005.06.290.

[63] WESSON, J., *Tokamaks*, Oxford University Press, 4 edition, 2011.